

Article

Study on Flow Distribution and Structure Optimization in a Mix Chamber and Diffuser of a CO₂ Two-Phase Ejector

Lixing Zheng ^{1,*}, Hongwei Hu ¹, Weibo Wang ¹, Yiyang Zhang ¹ and Lingmei Wang ²

¹ School of Electric Power, Civil Engineering and Architecture, Shanxi University, Taiyuan 030006, China; 202023504007@email.sxu.edu.cn (H.H.); 1811392018@st.gxu.edu.cn (W.W.); 202123504049@email.sxu.edu.cn (Y.Z.)

² Wind Turbine Monitoring and Diagnosis NTRC of Shanxi Province, Taiyuan 030006, China; wanglingmei@sxu.edu.cn

* Correspondence: lxzheng@sxu.edu.cn; Tel.: +86-0351-2646313

Abstract: This paper establishes a mathematic model of a CO₂ two-phase ejector to investigate flow distribution in the components of a mixing chamber and diffuser. The suction chamber was modeled using the characteristic line method to describe the development process of the supersonic expansion wave, and the mixing chamber, as well as diffuser models, were built based on the double-flow model. The reliability of the model was verified by experimental data. The distributions of flow parameters along the axis of the mixing chamber and diffuser were analyzed under different expansion ratios of the ejector. Structure optimizations of the mixing chamber and diffuser were conducted. The results showed that the primary flow temperature gradually increased along the axis of the mixing chamber and diffuser, but the Mach number distribution decreased for a certain ejector expansion ratio. The temperature and Mach number of the secondary flow showed the opposite trend. Moreover, at the initial stage of mixing, the fluid pressure increased rapidly, and the Mach number of the primary flow decreased rapidly. The gas-phase fraction of primary flow increased gradually in the mixing chamber and was stable in the diffuser. When the length–diameter ratio of the mixing chamber was about 10.8–12, it was beneficial to mix uniformity, and when the expansion angle of the diffuser was 4–6°, the ejector had a better ejector efficiency.

Keywords: CO₂ ejector; flow distribution; characteristic line method; distribution parameter method; structure optimization

MSC: 76-10; 80A05



Citation: Zheng, L.; Hu, H.; Wang, W.; Zhang, Y.; Wang, L. Study on Flow Distribution and Structure Optimization in a Mix Chamber and Diffuser of a CO₂ Two-Phase Ejector. *Mathematics* **2022**, *10*, 693. <https://doi.org/10.3390/math10050693>

Academic Editor: Simeon Reich

Received: 27 January 2022

Accepted: 21 February 2022

Published: 23 February 2022

Publisher's Note: MDPI stays neutral with regard to jurisdictional claims in published maps and institutional affiliations.



Copyright: © 2022 by the authors. Licensee MDPI, Basel, Switzerland. This article is an open access article distributed under the terms and conditions of the Creative Commons Attribution (CC BY) license (<https://creativecommons.org/licenses/by/4.0/>).

1. Introduction

Recently, ejectors have been subject to great focus in energy systems, the process industry and low-grade heat use, by virtue of its advantages of saving energy and its simple structure. Nevertheless, due to the complex flow characteristics in the CO₂ ejector, it is particularly difficult to comprehensively understand the flow behavior in each part, including the motive nozzle, suction chamber, mixing chamber, and diffuser [1,2]. Numerous scholars have carried out many theoretical analyses and numerical simulations on ejectors [3,4]. Palacz and Haida et al. [5–7] conducted a series of studies to continuously perfect the delay equilibrium model (DEM) and homogeneous equilibrium model (HEM) of a CO₂ ejector, and obtained abundant field information to optimize the ejector structure. Nakagawa et al. [8] established a CO₂ supersonic two-phase model based on HEM, and discussed how the shockwave changes. Although the above-mentioned CFD models have advantages in the evaluation of detailed flow field inside the ejector, numerical techniques are time-consuming and need powerful computers, and it is not easy to deal with the stability criteria [9]. By contrast, the reasonable one-dimensional thermodynamic model is more computationally cheap and operationally reliable. Li et al. [10] studied two-phase

flow in a transcritical CO₂ ejector using a visualization experiment. Based on the isentropic expansion process of primary flow, the transition position of the phase change was discovered by experiment and theoretical analysis. Banasiak et al. [11] constructed a CO₂ ejector model where the control equations were developed for the mixing chamber and diffuser to obtain internal flow distribution characteristics. Chen et al. [12] used the characteristic line method to study the Mach wave structure of primary flow and predicted the flow pattern in the ejector, and pointed out that the influence of the Mach wave should be considered under off-design conditions. Though many CO₂ ejector models have been established based on the thermodynamic method or gas dynamic method, the suction chamber model is usually constructed based on the zero-dimension model, given the lack of the understanding of the expansion wave and flow distribution analysis [11]. In addition, the condensation and entrainment of fluid in the mixing process increases the difficulty of analyzing mass and energy transfer. Therefore, it is necessary to investigate the distribution of thermodynamic parameters along the flow path of an ejector to further improve ejector performance.

The theoretical analysis of flow characteristics is an effective method for guiding geometry optimization [13,14]. Many studies have been conducted to optimize the structural parameters of the ejector [15–17]. Yan et al. [18] numerically and experimentally improved the convergence angle of a suction chamber and an optimized convergence angle improved the entrainment ratio of ejector by 15%. Wu et al. [19] found that there was an optimal convergence angle and length of mixing chamber for achieving the best ejector performance by virtue of CFD simulation. Yan et al. [20] improved mixing performance of the ejector by simulating key ejector geometric parameters such as the length of the constant pressure-mixing section and the length of the constant area-mixing section. Li et al. [21,22] proposed the optimal length–diameter ratio of the ejector mixing chamber by comparing the difference in shockwave lengths. Kandakure et al. [23] explored the structure of the mixing chamber and found the length–diameter ratio of the mixing chamber had a strong impact on internal flow loss and efficiency of the ejector. Balamurugan et al. [24] provided the optimal matching range between the mixing chamber length–diameter ratio as well as the semi-cone angle of the diffuser and the nozzle outlet velocity to reduce operating costs. A too-large or too-small semi-cone angle and inappropriate length of diffuser was found to be counterproductive for improving the performance of the ejector. Although there are many studies that have investigated ejector geometry, only a few radial dimensions have been discussed and determined by theoretical deduction. Axial dimensions, including nozzle exit position and lengths of mixing chamber and diffuser, are rarely determined by theoretical foundation. In particular, the lengths of the mixing chamber and diffuser, which achieves momentum and heat transfer, should be studied in more depth. At present, the lengths of mixing chamber and diffuser are mainly decided by the empirical formula summarized from experimental data [25]. However, the universality of the empirical formula is also problematic for different working conditions and working media. Even so, an in-depth study of flow distribution in the mixing chamber and diffuser can provide important theoretical references for the analysis of energy and mass transfer, as well as irreversible loss.

In this paper, a global mathematical model of a CO₂ two-phase ejector was established, in which the suction chamber model was developed using the characteristic line method, focusing on supersonic expansion of primary flow, and the mixing chamber and diffuser was modeled using the double-flow model to obtain the flow distribution characteristics in the mixing process. Based on the experimental structural and thermodynamic parameters of the CO₂ ejector, the variation of flow parameters, such as temperature, velocity, Mach number and pressure in the ejector, were analyzed, and optimization strategies regarding the length–diameter ratio of the mixing chamber and semi-cone angle of the diffuser were proposed.

2. Mathematical Model

2.1. Motive Nozzle and Suction Chamber

Figure 1 gives a schematic diagram of the ejector. To simplify the calculation of the motive nozzle and suction chamber, the following assumptions have been made: (1) the fluid flow in the motive nozzle is a one-dimensional steady adiabatic flow; (2) the motive nozzle is a converge nozzle; (3) the two fluids in the suction chamber are coaxial flow, and do not mix; (4) the velocity of primary flow and secondary flow at the ejector inlet is ignored; (5) thermal diffusion and turbulent viscous heat transfer are ignored. Therein, the converging nozzle is assumed to be correctly validated by the experimental data, which is tested based on this kind of nozzle [26].

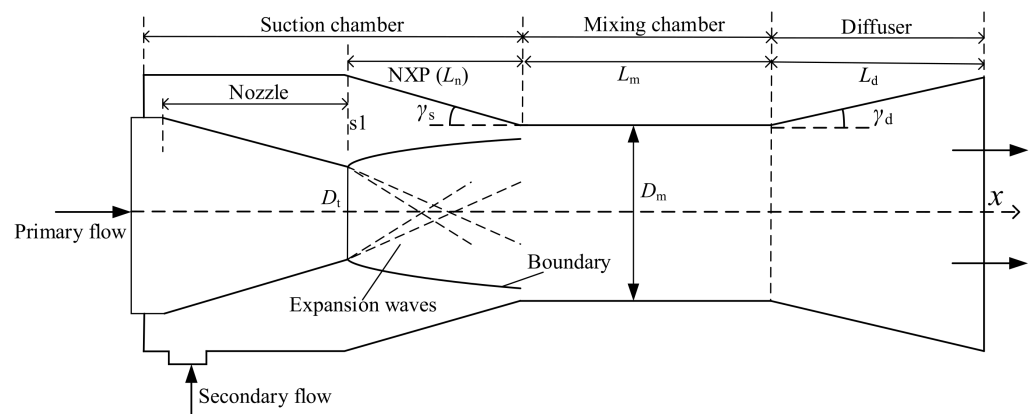


Figure 1. Schematic diagram of ejector structure.

The primary flow inlet pressure p_p and temperature T_p are the known parameters, and inlet enthalpy h_p and thermodynamic entropy s_p are obtained by REFPROP [27]. Assuming the nozzle outlet pressure p_t , the enthalpy at nozzle outlet h_t is obtained by isentropic flow between the nozzle inlet and outlet. The energy conservation in the nozzle is used to determine the nozzle outlet velocity V_t :

$$h_t = h_p - \eta_n (h_p - h_t) \tag{1}$$

$$V_t = \sqrt{2(h_p - h_t)} \tag{2}$$

where η_n is the nozzle efficiency, which is evaluated according to [26]. As the primary flow is choked at the nozzle throat, the sound velocity V_c at the nozzle outlet is compared with the V_t , and the outlet pressure p_t is constantly updated until the velocities converge. Considering that the exit of the motive nozzle is a two-phase flow, the sound velocity model presented by [28] is adopted to consider the non-equilibrium phase transformation.

To describe the expansion wave of primary flow in the suction chamber, the characteristic line method is used to solve the Mach line and node parameters of the expansion wave region to obtain the flow parameters in the suction chamber. The characteristic line method is commonly employed in simulations involving supersonic flow, to calculate the flow parameters along the characteristic curve direction. The perturbation in the supersonic flow field always spreads along the Mach line, while the Mach line is the characteristic line of supersonic flow field. Based on characteristic line method, a more accurate numerical solution can be obtained. In addition, because the finite differential method is adopted, the expansion wave and shockwave are considered to be simple waves, which can be described by the characteristic curve.

Though the thermophysical properties of CO_2 would impart dramatic changes at the critical point, if the real-time thermophysical properties are used in the model calculation, it must affect the robustness of the simulations. Thus, the gas dynamics equations are established based on the isentropic relationship and mass conservation, which is the

commonly accepted approach for shockwave prediction, and it can guarantee that the simulation robust.

It is assumed that the fluid at the nozzle outlet flows axially, and its half-amplitude expansion region is the A_1OA_{11} region, as shown in Figure 2. The expansion region is considered to be composed of many weak expansion waves, each of which is along the Mach line. The A_1A_{11} line in Figure 2 shows a Mach line in the first expansion wave at the outlet of the primary flow nozzle. Since all flow parameters are the same along the Mach lines in the expansion wave, and the Mach lines are straight, the Mach line A_1A_{11} can be evenly divided into several points.

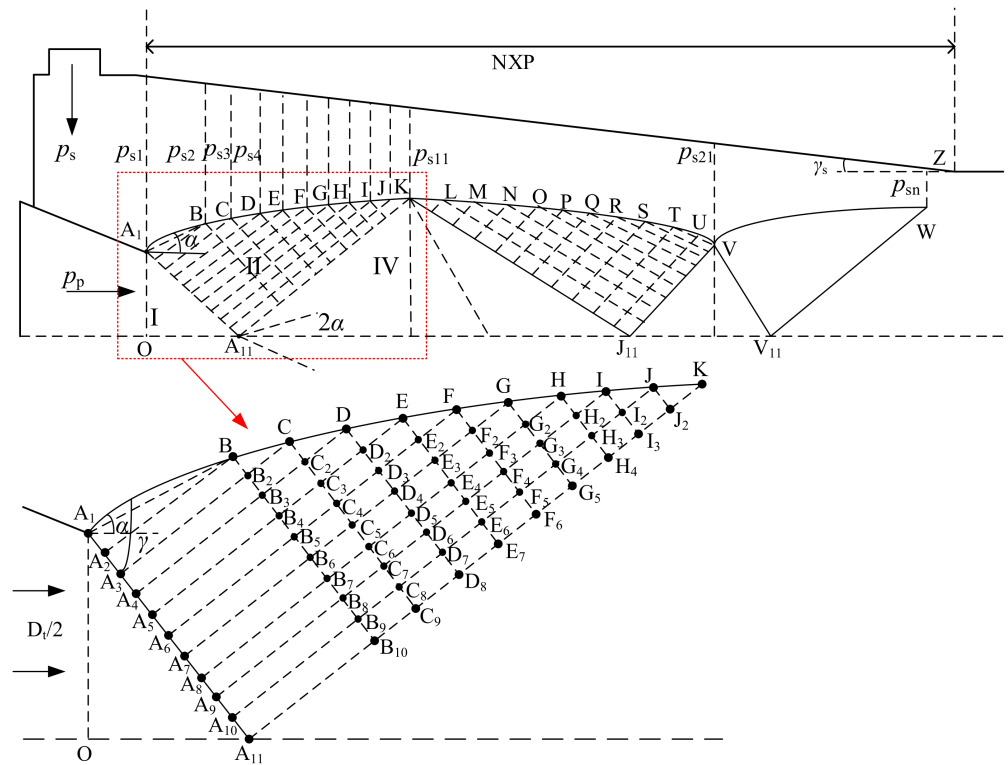


Figure 2. Grid of characteristic lines at the motive nozzle outlet of the primary flow.

Since the flow is deflected counterclockwise after passing through the expansion wave, the expansion wave system A_1OA_{11} is a right-extension expansion wave, and the expansion angle α of the flow can be obtained by Prandtl–Meyer function [29]:

$$\alpha = v(Ma_{p,s1}) - v(Ma_t) \tag{3}$$

where Ma_t and $Ma_{p,s1}$ are the Mach numbers of the primary flow at the nozzle outlet before and after the expansion wave, respectively. According to the isentropic flow, the Mach number $Ma_{p,s1}$ can be obtained as follows:

$$\frac{p_t}{p_{p,s1}} = \left(1 + \frac{k-1}{2} Ma_{p,s1}^2\right)^{\frac{k}{k-1}} \tag{4}$$

Herein, due to the adiabatic isentropic flow, the boundary pressure of primary flow at post-wave $p_{p,s1}$ is equal to the pressure of the secondary flow at Section s1 p_{s1} . The corresponding Mach angle γ_{ma} is expressed as:

$$\gamma_{ma} = \arcsin(1/Ma_{p,s1}) \tag{5}$$

The slope of Mach line A_1A_{11} can be calculated by:

$$k = \tan(\alpha - \gamma) \tag{6}$$

According to the coordinates of point A_1 and the slope of Mach line A_1A_{11} , the equation of Mach line A_1A_{11} is solved. According to the two-phase flow sound velocity model, the local sound velocity V_c at the outlet of the primary flow in nozzle is calculated. Then, the velocity of the primary flow after the first expansion wave system $V_{p,s1}$ is given as:

$$V_{p,s1} = Ma_{p,s1} V_c \tag{7}$$

Then the axial velocity u_{A1} and radial velocity v_{A1} of fluid at each point of Mach line A_1A_{11} are expressed, respectively as:

$$u_{A1} = V_{p,s1} \cos \alpha \tag{8}$$

$$v_{A1} = V_{p,s1} \sin \alpha \tag{9}$$

The position information and flow parameters of point B are obtained by the solving approach of the free pressure boundary points of the characteristic line method. Then, the subsequent position and flow parameters of point B_2 are also calculated using the finite difference method. Similarly, the spatial positions and flow parameters of all nodes in the $A_1A_{11}K$ region are solved.

Because both the upper and lower edges of the nozzle outlet would generate expansion waves, two bunches of new expansion waves are produced to maintain the pressure balance after the expansion wave. Subsequently, the fluid flows inward and close to the middle axis, forming the compression wave. Then, expansion waves and compression waves appear alternately, forming a brick-like shockwave chain.

Since the inlet parameters of the secondary flow are known, according to the isentropic relationship and energy conservation between the inlet section of the ejector and Section s1 (as shown in Figure 1), the Mach number, density and velocity of the secondary flow at Section s1 can be obtained by assuming the pressure p_s :

$$\frac{p_s}{p_{s,s1}} = \frac{\rho_s}{\rho_{s,s1}} = \left(1 + \frac{k-1}{2} Ma_{s,s1}^2\right)^{\frac{k}{k-1}} \tag{10}$$

$$u_{s,s1} = \sqrt{2(h_s - h_{s,s1})} \tag{11}$$

$$h_{s,s1} = h_s - \eta_s(h_s - h_{s,s1}) \tag{12}$$

where k is the adiabatic index, and η_s is the suction chamber efficiency, which is referred to in [26].

According to the mass conservation of the secondary flow, the density could be expressed as:

$$\rho_{s,si} u_{s,si} A_{s,si} = \rho_{s,s(i+1)} u_{s,s(i+1)} A_{s,s(i+1)} \tag{13}$$

In addition, based on the Bernoulli equation, the fluid pressure is defined as:

$$\frac{k}{k-1} \frac{p_{s,si}}{\rho_{s,si}} + \frac{u_{s,si}^2}{2} = \frac{k}{k-1} \frac{p_{s,s(i+1)}}{\rho_{s,s(i+1)}} + \frac{u_{s,s(i+1)}^2}{2} \tag{14}$$

According to Equation (10), the Mach number $Ma_{s,s1}$ and density $\rho_{s,s1}$ of the secondary flow in Section s1 have been obtained. The density $\rho_{s,s2}$, Mach number $Ma_{s,s2}$ and velocity $u_{s,s2}$ in Section s2 are determined using the continuity and energy conservation equation as well as isentropic flow. Combining Equations (13) and (14), $p_{s,s2}$ can be solved, and $p_{s,sn}$ is iterated. In return, the pressure, velocity, Mach number and density of the secondary flow along the flow axis can be obtained.

The primary flow expands and compresses alternately, and the flow deflection angle also changes continually. Based on the Prandtl–Meyer function and the deflection angle of the primary flow in each region, the Mach number along the axis can be determined by iterative calculation, where the pressure of the primary flow is consistent with the secondary flow pressure as the iterative convergence condition. In addition, then, the primary flow pressure $p_{p,pn}$ along the axis can be obtained.

2.2. Mixing Chamber and Diffuser Model

The distributed parameter method is used to model the mixing chamber and diffuser, where the mixing chamber and diffuser is divided into many elements along the flow path. The double-flow model is used where the primary stream flow in the center and the suction stream flow annularly. The partial differential governing equations of mass, momentum and energy are established on each element. To facilitate the construction of mixing chamber and diffuser model, the following assumptions are made [11]:

- The fluid in the mixing chamber and diffuser is the steady flow state.
- The external forces are ignored.
- The mass transfer between the two streams is calculated by the condensation and entrainment.
- The momentum transfer is determined by the drag forces of interface between the two streams and the mass transfer resulted in the momentum gain or loss.
- The friction pressure drop is accounted for by the wall boundary layer and the imaginary mixing layer between the two streams.

According to the above hypothesis, the mass equation is determined by:

$$\frac{d}{dl}(\rho_j A_j u_j) = \Gamma_j \tag{15}$$

$j \in (1, 2)$, 1 represents the primary flow and 2 represents the secondary flow. Γ_j is the mass transfer differential at the interface between the primary flow and the secondary flow, which mainly includes the mass transfer differential Γ_c generated by the condensation of the primary flow to the secondary flow, and the mass transfer differential generated by the primary flow entraining secondary flow Γ_{2-1} , as well as the mass transfer differential Γ_{1-2} generated by the deposition of the primary flow to secondary flow, since the deposition of primary flow to secondary flow is not considered, $\Gamma_{1-2} = 0$.

The mass differential formula for condensation of primary flow to secondary flow is expressed as [30]:

$$\Gamma_c = \frac{\alpha_{int}(T_1 - T_2)}{h_{int} - h_{1,sat}} \frac{dF_{int}}{dl} \tag{16}$$

The mass transfer differential Γ_{2-1} generated by the primary flow entraining secondary flow is calculated by the following equation [11].

$$\Gamma_{2-1} = \begin{cases} 1.175 \times 10^{-4} \times u_1 \sqrt{\rho_1 \rho_2} \eta_2 (Re_2 - Re_{2,\infty}) & (Re_2 \geq Re_{2,\infty}) \\ 0 & (Re_2 < Re_{2,\infty}) \end{cases} \tag{17}$$

where Re_2 is the Reynolds number of secondary flow, $Re_{2,\infty}$ is the local equilibrium Reynolds number, and the calculation formula is as follows:

$$Re_{2,\infty} = \exp\left(5.8504 + 0.4249 \frac{\mu_1}{\mu_2} \sqrt{\frac{\rho_2}{\rho_1}}\right) \tag{18}$$

Therefore, the mass equation of the primary flow is expressed as:

$$\frac{d}{dl}(\rho_1 A_1 u_1) = \Gamma_1 = \Gamma_{2-1} - \Gamma_c \tag{19}$$

The mass equation of the secondary flow has the following form:

$$\frac{d}{dl}(\rho_2 A_2 u_2) = \Gamma_2 = \Gamma_c - \Gamma_{2-1} \tag{20}$$

The momentum equation of primary flow is as follows:

$$A_1 \rho_1 u_1 \frac{du_1}{dl} + A_1 \frac{dp}{dl} = (\Gamma_{2-1} - \Gamma_c)(u_{1,int} - u_1) + M_{1,int} - F_{1,w} \tag{21}$$

where $M_{1,int}$ is the momentum transfer differential at an interface between the primary flow and the secondary flow:

$$M_{1,int} = -0.5C_{1-2}\rho_1(u_1 - u_2)|u_1 - u_2|\frac{dF_{1,int}}{dl} \tag{22}$$

$F_{1,w}$ is the friction differential at the interface between the primary flow and the secondary flow:

$$F_{1,w} = \frac{f_{1,w}}{2}\rho_1(u_1 - u_2)^2\frac{dF_{1,int}}{dl} \tag{23}$$

C_{1-2} is the interface resistance coefficient of primary flow and secondary flow, calculated by:

$$C_{1-2} = b \left[\frac{\rho_2}{\mu_2}(u_1 - u_2)D\sqrt{\frac{A_1}{A_1 + A_2}} \right]^{-0.25} \tag{24}$$

where b is the scale factor, which is measured experimentally.

The momentum equation of the secondary flow can be obtained as follows:

$$A_2 \rho_2 u_2 \frac{du_2}{dl} + A_2 \frac{dp}{dl} = (\Gamma_c - \Gamma_{2-1})(u_{2,int} - u_2) + M_{2,int} - F_{2,w} \tag{25}$$

where $M_{2,int}$ is the friction differential between the primary flow and the secondary flow:

$$M_{2,int} = 0.5C_{1-2}\rho_1(u_1 - u_2)|u_1 - u_2|\frac{dF_{1,int}}{dl} \tag{26}$$

$F_{2,w}$ is the friction differential at the wall surface, expressed as follows:

$$F_{2,w} = \frac{f_{2,w}}{2}\rho_2 u_2^2 \frac{dF_w}{dl} \tag{27}$$

The friction coefficient of single-phase flow is given as the following:

$$\frac{1}{\sqrt{f_k}} = 2\lg(Re\sqrt{f_k}) - 0.8 \tag{28}$$

The friction coefficient of two-phase flow is calculated by the Churchill model [31].

The energy equations of two streams are expressed, respectively:

$$A_1 u_1^2 \rho_1 \frac{du_1}{dl} + A_1 u_1 \rho_1 \frac{dh_1}{dl} = (\Gamma_{2-1} - \Gamma_c) \left(h_{1,int} - h_1 + \frac{u_{1,int}^2}{2} - \frac{u_1^2}{2} \right) \tag{29}$$

$$A_2 u_2^2 \rho_2 \frac{du_2}{dl} + A_2 u_2 \rho_2 \frac{dh_2}{dl} = (\Gamma_c - \Gamma_{2-1}) \left(h_{2,int} - h_2 + \frac{u_{2,int}^2}{2} - \frac{u_2^2}{2} \right) \tag{30}$$

In addition, the geometric relationship is showed as follows:

$$\frac{dA_m}{dl} = \frac{dA_1}{dl} + \frac{dA_2}{dl} \tag{31}$$

Combining Equations (19)–(21), (25) and (29)–(31), a 9-order control equation including state and structural parameters of primary flow and secondary flow is developed, and its independent variable parameters are expressed as: $x = \left[\frac{du_1}{dt}, \frac{du_2}{dt}, \frac{dh_1}{dt}, \frac{dh_2}{dt}, \frac{d\rho_1}{dt}, \frac{d\rho_2}{dt}, \frac{dA_1}{dt}, \frac{dA_2}{dt}, \frac{dp}{dt} \right]$. Using the fourth-order Runge–Kutta method, the fluid state parameters along the flow path of the primary flow and the secondary flow in the mix chamber and diffuser can be obtained. The specific calculation steps of the mixing chamber and diffuser are given as follows: first, the fluid parameters calculated by the motive nozzle and suction chamber are taken as the initial boundary parameters of the inlet of the mixing chamber, such as pressure, velocity, temperature, cross-sectional area and enthalpy. Then, the variables $\Gamma_c, \Gamma_{2-1}, F_{1,int}, F_{1,w}, F_{2,w}$ are calculated. In the end, the 9-order control equation for every element is solved to obtain the pressure, velocity, enthalpy, density, and cross-sectional area.

3. Model Validation

The authors carried out experimental tests on the transcritical CO₂ ejector expansion refrigeration system with an adjustable structure ejector, and the performance parameters of the ejector under different NXP and the motive nozzle throat area are obtained [26,30]. In addition, among the calculations of the differential of interface momentum transfer rate $M_{1,int}$ presented in Section 2.2, the scale coefficient b in the interface drag coefficient C_{1-2} is confirmed to be 1.5. The heat transfer coefficient between the primary flow and suction flow refers to the study by Hwang and is amended with the operating conditions [32]. During the calculation of differential of mass transfer F_{2-1} , the kinetic viscosity of suction flow is adjusted for the working conditions.

Here, the entrainment ratio μ and the ejector outlet pressure p_c calculated by the present model are compared with the above experimental data to verify mode accuracy. Figure 3 shows that the maximum deviation, minimum deviation, and average deviation of the entrainment ratios between the model calculation value and the experimental measurement are 12.21%, 0.37%, and 4.93%, respectively. To compare the ejector outlet pressure p_c , as shown in Figure 4, the maximum deviation, minimum deviation, and average deviation are 4.48%, 0.025%, and 1.55%, respectively. The deviation is mainly due to the machining accuracy of ejector, the influence of friction, and heat transfer model; however, the calculation error is within the allowable range.

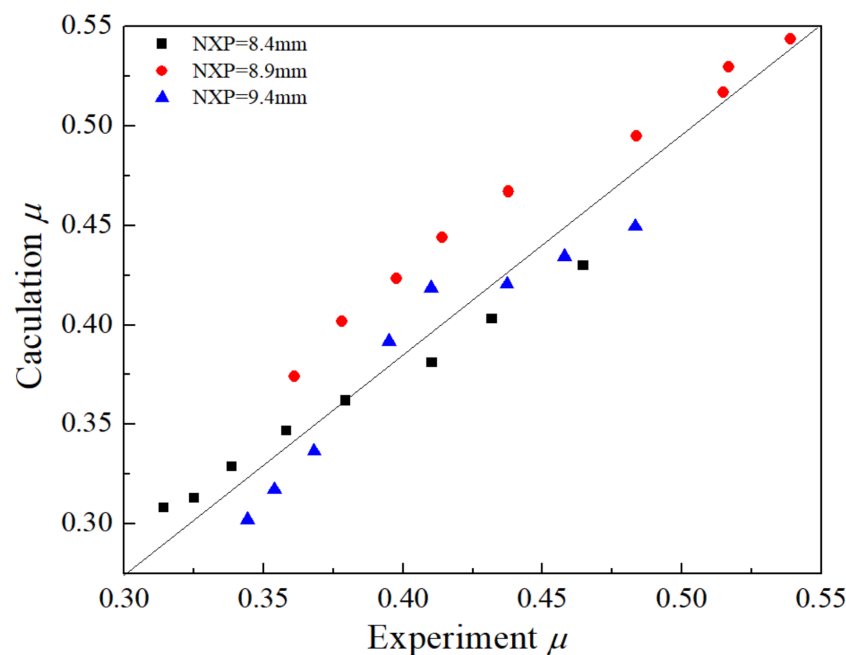


Figure 3. Comparison between calculated and experimental entrainment ratio μ .

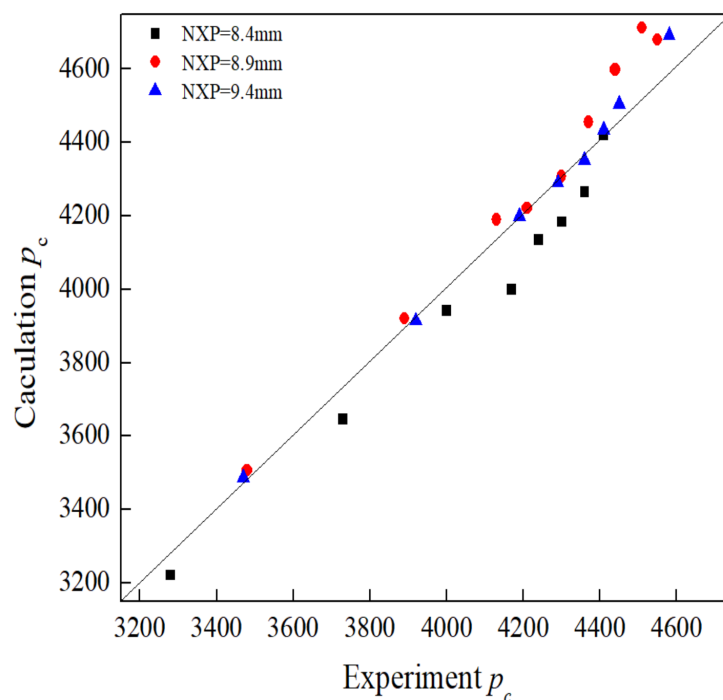


Figure 4. Comparison between calculated and experimental pressure p_c .

4. Result and Discussion

4.1. Flow Distribution

According to the structural and flow parameters of the CO₂ ejector tested in [26,30], in this paper, five groups of expansion ratios p_p/p_s (ratio of primary flow pressure to secondary flow pressure) are selected to analyze the flow distribution in the mixing chamber and diffuser. The specific experimental data can be found in [26,30].

Figure 5 shows the temperature distribution of the primary flow and secondary flow along the path of the mixing chamber and diffuser under different expansion ratios p_p/p_s . The temperature of the primary flow is represented with a solid line, and for the secondary flow a dashed line. It can be seen from Figure 5 that the temperature of the primary flow along the path gradually increases, while the temperature of the secondary flow gradually decreases, and the temperatures of the two fluids tend to be equal in the flow process. This is mainly due to the supersonic expansion of the primary flow in the nozzle and the suction chamber, resulting in its temperature lower than that of the secondary flow. In the process of energy transfer between the two streams in the mixing chamber and diffuser, the secondary flow will condense and release heat into the primary flow, making the temperature of primary flow rise until the temperature of the two streams reaches equilibrium. Moreover, the temperature difference between the two streams at the entrance of mixing chamber is largest, which accelerates the energy transfer rate. In addition, for the small expansion ratio, the temperature of primary flow rises rapidly at the initial stage of mixing, while the large expansion ratio makes the secondary flow temperature decrease significantly in the mixing process. The final temperature difference between the two streams is 2.4 K at high expansion ratio ($p_p/p_s = 2.77$), and it is higher than that at low expansion ratio ($p_p/p_s = 1.95$) where the temperature difference is only 0.32 K. Due to the limitations of existing ejector structure, the energy exchange between two streams cannot be completed in a limited space. Therefore, it is necessary to optimize the mixing process of the ejector to improve energy transfer efficiency.

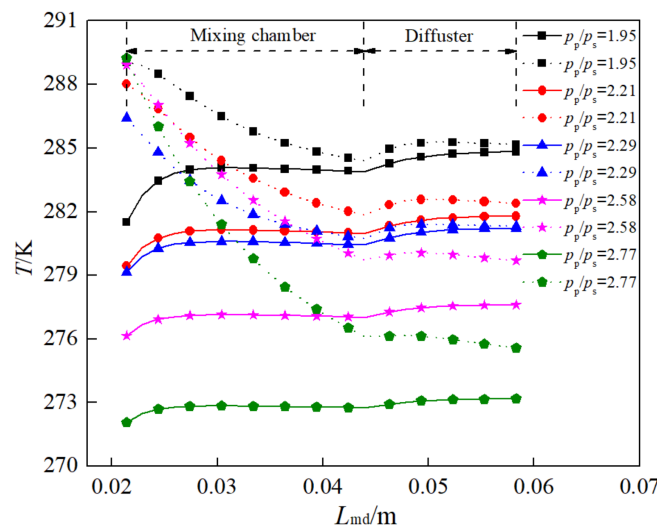


Figure 5. Temperature distribution along the path of the mixing chamber and diffuser.

Figure 6 shows the Mach number distribution of the primary flow and secondary flows along the path of the mix chamber and diffuser under different expansion ratios p_p/p_s . From Figure 6 it can be seen that the primary flow is in a supersonic state at the beginning of the mixing process, and the Mach number of primary flow decreases gradually, falling fastest in the initial stage of mixing chamber (the top 15% of the total length). More specifically, under the five groups of expansion ratio, the declines of Mach number at the initial stage of the mixing chamber, accounting for the whole process, are 74.6%, 73.7%, 74.2%, 76.6% and 80.8%, respectively. In the diffuser, the Mach number of the primary flow decreases more obviously than in the secondary flow, and the Mach number differences between the two fluids decrease gradually. At the beginning of the mixing chamber, the supersonic velocity of the primary flow is much larger than that of the secondary flow, and the momentum transfers of the two fluids results in the rapid decrease in the primary flow velocity in the limited mixing space. After entering the diffuser, the velocity of both fluids decreases significantly. Moreover, there is still a gap of the Mach numbers between the two fluids at the diffuser, which indicates that there is still room for further improvement to the ejector used in the experiment. Moreover, the larger velocity difference between the two streams leads to evident velocity slip, and this is accompanied by the larger Reynolds number [33]. In addition, a favorable heat transfer occurs, which has similar conclusions to that of Figure 5.

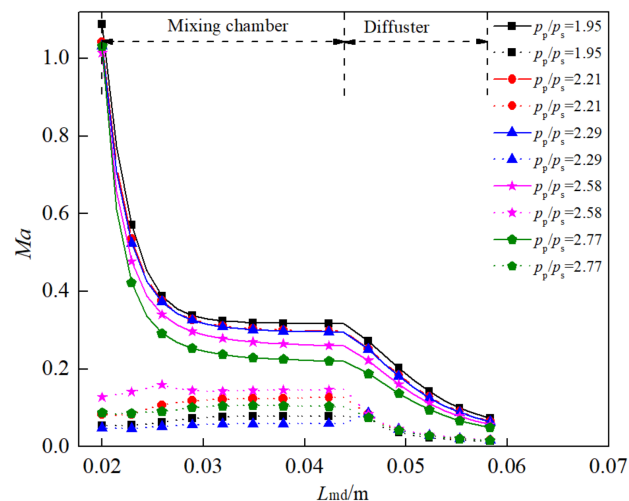


Figure 6. Mach number distribution along the mixing chamber and diffuser.

Figure 7 shows the pressure distribution along the mixing chamber and diffuser under different expansion ratios p_p/p_s . At the initial stage of the mixing chamber, the fluid pressure increases rapidly, and at the five expansion ratios, the pressure increase at the initial stage of the mixing chamber (the first 15% of the total length of the mixing chamber) accounts for 73.7%, 69.3%, 67.2%, 65.1%, and 63.9% of the total pressure increase, respectively. With the increase in expansion ratio, the proportion of pressure lift in the initial stage of the mixing chamber decreases gradually. In the diffuser, the pressure increase is more obvious at a smaller expansion ratio. It can be seen that the pressure lift at the initial stage of the mixing chamber is obvious, but in the final one it decreases in the case of a large expansion ratio. This is reasonable because the velocity difference between the two streams increases with the decline of expansion ratio, as shown Figure 6. When the fluid enters the mixing chamber, the flow cross-sectional area decreases, and more kinetic energy is transformed to pressure energy for a smaller expansion ratio. Thus, the smaller expansion ratio is helpful for increasing mixing pressure.

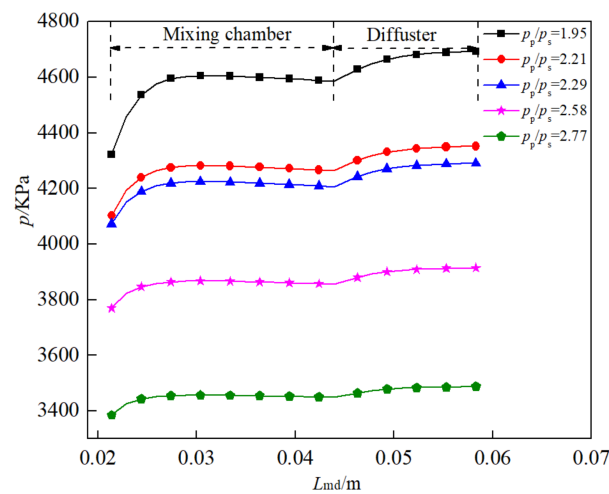


Figure 7. Pressure distribution along the path of the mixing chamber and diffuser.

Figure 8 shows the distribution of the gas-phase mass fraction of the primary flow q_m along the path of the mixing chamber and diffuser under different expansion ratios p_p/p_s . The gas-phase mass fraction q_m increases gradually along the path of the mixing chamber and diffuser, and the largest increase is in the mixing chamber. This is because when just entering the mixing chamber, the temperature difference between the primary flow and the secondary flow is large, which accelerates energy transfer. The primary flow temperature increases, and leads to an increase in gas-phase mass fraction of primary flow q_m . After entering the diffuser, the temperature difference between the two streams is relatively small, and the increase range of q_m decreases. In addition, a larger expansion ratio of p_p/p_s leads to a larger increase in q_m . The foremost reason for this is that the large temperature difference between the two streams under a large expansion ratio makes energy exchange more intense and leads to a larger increase in q_m .

Figure 9 shows the mass distribution of the two streams in the mixing chamber and diffuser when the expansion ratio $p_p/p_s = 1.95$. The mass flow rate of primary flow m_p gradually increases, while the mass flow rate of the secondary flow m_s decreases. Combined with Figure 5, it can be seen that in the mixing chamber and diffuser, the temperature of the secondary flow is always higher than that of the primary flow, resulting in the condensation of the secondary flow. At the same time, it can be seen from Figure 6, in the mixing process of the two streams, that the primary flow velocity is faster than that of the secondary flow, and the primary flow would entrain the secondary flow. This mass transfer is caused by condensation and entrainment between the two fluids that leads to an increase in the mass flow rate of primary flow m_p and the decrease in the mass flow rate of secondary flow m_s .

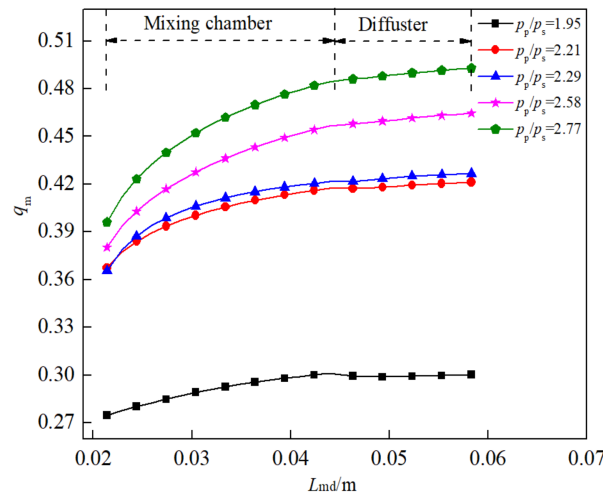


Figure 8. The gas-phase mass fraction distribution in the mixing chamber and diffuser.

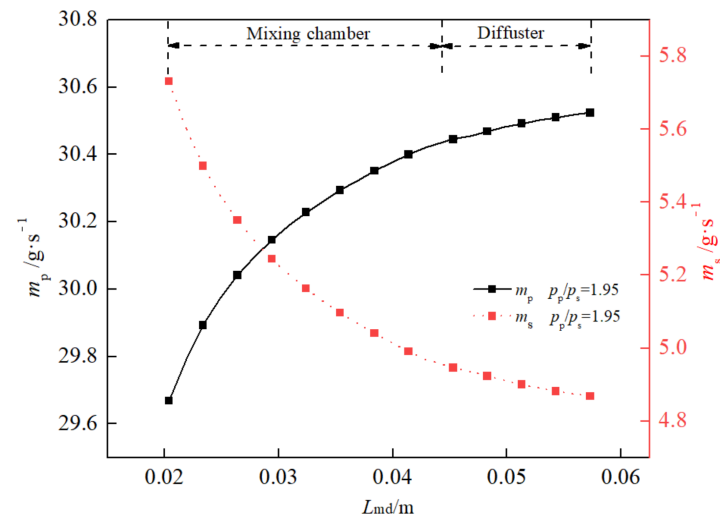


Figure 9. Fluid mass distributions along the mixing diffuser chamber.

4.2. Optimization of Mixing Chamber Length

According to the above analysis, an optimization method of mixing chamber length is now investigated. We keep the diameter of the mixing chamber and other operating parameters unchanged as per experimental tests in [26,30]. The length of mixing chamber L_m is calculated under different expansion ratio p_p/p_s . Figure 10 shows the relationship between the velocity difference of two fluids at the mixing chamber exit and the length-diameter ratio of the mixing chamber L_m/D_m . It can be seen from Figure 10 that when the ejector expansion ratio remains unchanged, the velocity difference ΔV decreases first and then increases with the increase in the length-diameter ratio of the mixing chamber L_m/D_m . When the velocity difference between the two streams is the smallest, the two fluids are mixed more fully at this time, and the corresponding mixing chamber length is considered to be the optimal value. In the calculation range, when L_m/D_m is about 10.8–12, the exit velocity difference of the ejector mixing chamber is the smallest, and the mixing uniformity is better. Ref. [34] has recommended the L_m/D_m to be 5–10 from the perspective of ejector efficiency. Ref. [35] found the maximum value of entrainment ratio when L_m/D_m was near to 6.1. There are differences between the literature values and the present results, and this is mainly because of the diversity of working conditions and optimization objectives. In this present range, it is more favorable to mix with uniformity.

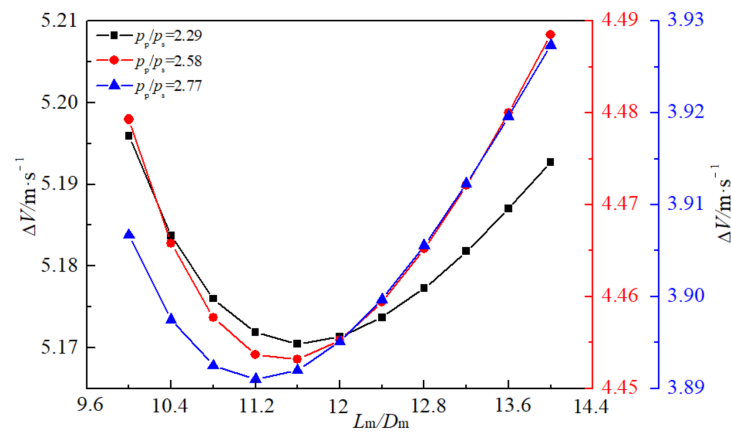


Figure 10. Influence of length–diameter ratio L_m/D_m on velocity difference of two fluids at the outlet of mixing chamber.

4.3. Optimization of Diffuser Angle

The diffuser is the last portion of the ejector, and the semi-cone angle and length of the diffuser have an important influence on the pressure lift of the ejector. A too-large or too-small semi-cone angle and inappropriate length of the diffuser would be counterproductive to improving the performance of the ejector. Therefore, the overall performance index of ejector efficiency η_{eje} is used to guide the optimization of the diffuser semi-cone angle γ_d , as shown in Figure 1. Figures 11 and 12 show the influence of the diffuser expansion angle γ_d on the ejector efficiency η_{eje} at different expansion ratios p_p/p_s , respectively. It can be seen from Figure 11 that with an increase in semi-cone angle γ_d , the efficiency η_{eje} increases first and then decreases, but the overall change is not obvious, and the ejector efficiency difference is small under different expansion ratios. Figure 12 shows that when the expansion ratio is constant, the ejector efficiency η_{eje} increases gradually with the increase in L_d/D_m , but the increase rate is small. For the ejector, the higher the ejector efficiency, the better the thermal performance, and its corresponding semi-cone angle is the best expansion angle. As can be seen from Figures 11 and 12, within the range of calculation, the optimal expansion angle ranges from 4–6°. Ref. [36] pointed out that there was an optimal range of diffuser divergence angle, and the best performances were recorded with an included angle of 5°. Ref. [34] also indicated the optimum diffuser divergence angle was between 3° and 5°. If the expansion angle is too large, an eddy in the boundary layer will be formed, and the static pressure recovery characteristics of the diffuser will be reduced. It is recommended that the semi-cone angle of the best performance of the diffuser is 5°, which is basically consistent with the conclusion of the present model in this paper.

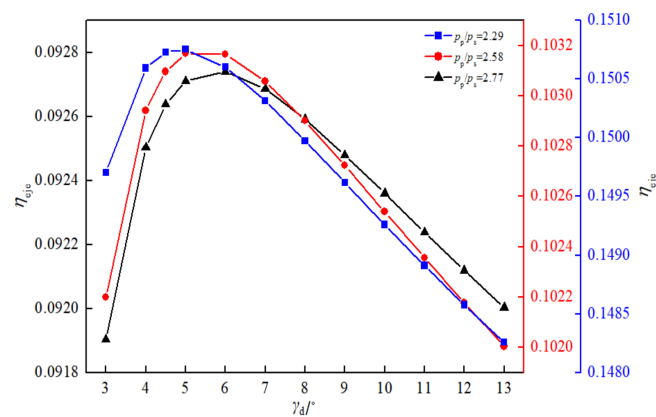


Figure 11. Effect of diffuser expansion angle γ_d on ejector efficiency η_{eje} under different expansion ratio p_p/p_s .

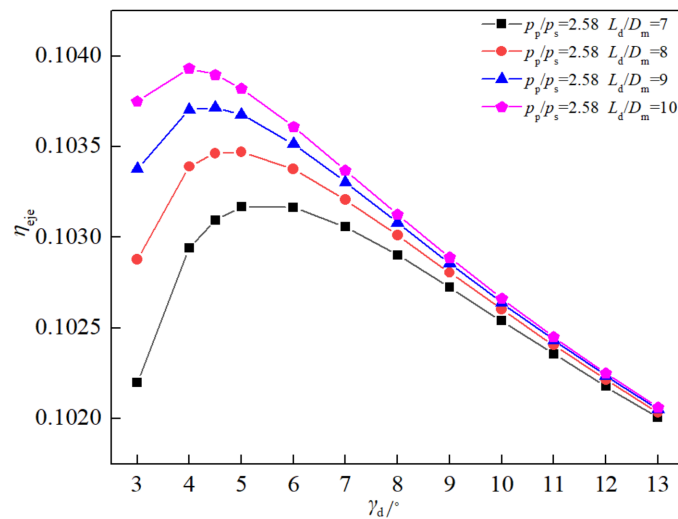


Figure 12. Effect of diffuser expansion angle γ_d on ejector efficiency η_{eje} under different L_d/D_m .

5. Conclusions

In this paper, a global mathematics model of a CO₂ ejector is established, where the suction chamber is modeled with the characteristic line method to describe the development process of a supersonic expansion wave, and the mixing chamber and diffusion model are developed using the double fluid model and distributed parameter method. The parameter distribution along the axis of the ejector including pressure, temperature, Mach number, mass fraction, and mass flow rate are presented. In addition, the length of the mixing chamber and the semi-cone angle of the diffuser are optimized based on the above distribution law. The most important findings of this investigation are summarized as follows:

- (1) The suction chamber model established by the characteristic line method is embedded into the global mathematical model of the CO₂ ejector. The expansion wave development in the suction chamber is considered, and its influence on the subsequent mixing process can be obtained. Compared with the experimental values presented in the literature [30], the average deviation of the entrainment ratio μ and the ejector outlet pressure p_c calculated by the present model are 4.93% and 1.55%, respectively.
- (2) In the mix chamber and diffuser, the temperature of the primary flow increases gradually along the path, while the Mach number and velocity decrease gradually, while the secondary flow shows an opposite trend. For the small expansion ratios, the temperature of the primary flow rises rapidly with the initial stage of mixing, while the large expansion ratio makes the secondary flow temperature decrease significantly in the mixing process. In the diffuser, the Mach number of the primary flow decreases more obviously than that of the secondary flow. The mass of the secondary flow is continuously transferred to the primary flow, and the gas-phase mass fraction of the primary flow increases gradually due to the transfer of energy and the rise of temperature.
- (3) The velocity difference between the two streams in the mixing chamber is proposed as the optimized parameter. It is found that the mixing uniformity is better when the length–diameter ratio of the mixing chamber is 10.8–12, and the ejector has a better ejector efficiency when the semi-cone angle of the diffuser is 4–6°.

Although the suction chamber model is established using the characteristic line method, it is based on the gas dynamic function and does not consider real gas physical properties. Additional research efforts on model optimization will be performed to improve prediction accuracy and extend the application range.

Author Contributions: Conceptualization, L.Z. and H.H.; methodology, L.Z., H.H. and W.W.; software, L.Z., H.H. and W.W.; validation, L.Z., H.H. and W.W.; formal analysis, H.H. and W.W.; investigation, H.H., W.W. and Y.Z.; resources, L.Z. and L.W.; data curation, L.Z., H.H. and W.W.; writing—original draft preparation, L.Z., H.H. and Y.Z.; writing—review and editing, H.H. and Y.Z.; visualization, H.H. and L.W.; supervision, L.Z. and L.W.; project administration, L.Z.; funding acquisition, L.Z. and L.W. All authors have read and agreed to the published version of the manuscript.

Funding: This research was funded by The National Natural Science Foundation of China, grant number 51806132 and Scientific and Technological Innovation of colleges and universities of Shanxi Province, grant number 201802011.

Data Availability Statement: The data presented in this study are available upon reasonable request from the corresponding author.

Conflicts of Interest: The authors declare no conflict of interest.

References

1. Ramesh, A.S.; Sekhar, S.J. Experimental and numerical investigations on the effect of suction chamber angle and nozzle exit position of a steam-jet ejector. *Energy* **2018**, *164*, 1097–1113. [[CrossRef](#)]
2. Bodys, J.; Smolka, J.; Palacz, M. Experimental and numerical study on the R744 ejector with a suction nozzle bypass. *Appl. Therm. Eng.* **2021**, *194*, 117015. [[CrossRef](#)]
3. Besagni, G.; Mereu, R.; Inzoli, F. Ejector refrigeration: A comprehensive review. *Renew. Sustain. Energy Rev.* **2016**, *53*, 373–407. [[CrossRef](#)]
4. Ker, A.; Ya, A.; Pg, B. A detailed review on CO₂ two-phase ejector flow modeling. *Therm. Sci. Eng. Prog.* **2020**, *20*, 100647. [[CrossRef](#)]
5. Palacz, M.; Smolka, J.; Fic, A.; Bulinski, Z.; Nowak, A.J.; Banasiak, K.; Hafner, A. Application range of the HEM approach for CO₂ expansion inside two-phase ejectors for supermarket refrigeration systems. *Int. J. Refrig.* **2015**, *59*, 251–258. [[CrossRef](#)]
6. Haida, M.; Smolka, J.; Hafner, A.; Ostrowski, Z.; Palacz, M.; Madsen, K.B.; Försterling, S.; Nowak, A.J.; Banasiak, K. Performance mapping of the R744 ejectors for refrigeration and air conditioning supermarket application: A hybrid reduced-order model. *Energy* **2018**, *153*, 933–948. [[CrossRef](#)]
7. Haida, M.; Smolka, J.; Hafner, A.; Palacz, M.; Banasiak, K.; Nowak, A.J. Modified homogeneous relaxation model for the R744 trans-critical flow in a two-phase ejector. *Int. J. Refrig.* **2018**, *85*, 314–333. [[CrossRef](#)]
8. Nakagawa, M.; Berana, M.S.; Harada, A. Shock waves in supersonic two-phase flow of CO₂ in converging-diverging nozzles. *HVACR Res.* **2009**, *15*, 1081–1098. [[CrossRef](#)]
9. Fardi, M.; Pishkar, I.; Alidousti, J.; Khan, Y. Numerical investigation of the MHD suction–injection model of viscous fluid using a kernel-based method. *Arch. Appl. Mech.* **2021**, *91*, 4205–4221. [[CrossRef](#)]
10. Li, Y.F.; Deng, J.Q.; Ma, L. Experimental study on the primary flow expansion characteristics in transcritical CO₂ two-phase ejectors with different primary nozzle diverging angles. *Energy* **2019**, *186*, 115839. [[CrossRef](#)]
11. Banasiak, K.; Hafner, A. 1D Computational model of a two-phase R744 ejector for expansion work recovery. *Int. J. Therm. Sci.* **2011**, *50*, 2235–2247. [[CrossRef](#)]
12. Chen, Z.Z.; Dang, C.; Hihara, E. Investigations on driving flow expansion characteristics inside ejectors. *Int. J. Heat Mass Transf.* **2017**, *108*, 490–500. [[CrossRef](#)]
13. Yan, J.; Li, S.; Liu, Z. Numerical investigation on optimization of ejector primary nozzle geometries with fixed/ varied NXP. *Appl. Therm. Eng.* **2020**, *175*, 115426. [[CrossRef](#)]
14. Barta, R.B.; Dhillon, P.; Braun, J.E. Design and optimization strategy for ejectors applied in refrigeration cycles. *Appl. Therm. Eng.* **2021**, *189*, 116682. [[CrossRef](#)]
15. Elbel, S.; Hrnjak, P. Experimental validation of a prototype ejector designed to reduce throttling losses encountered in transcritical R744 system operation. *Int. J. Refrig.* **2008**, *31*, 411–422. [[CrossRef](#)]
16. Chong, D.T.; Yan, J.J.; Wu, G.S. Structural optimization and experimental investigation of supersonic ejectors for boosting low pressure natural gas. *Appl. Therm. Eng.* **2009**, *29*, 2799–2807. [[CrossRef](#)]
17. Wen, H.; Yan, J. Effect of mixing chamber length on ejector performance with fixed/ varied area ratio under three operating conditions in refrigerated trucks. *Appl. Therm. Eng.* **2021**, *197*, 117379. [[CrossRef](#)]
18. Yan, J.; Cai, W.; Li, Y. Geometry parameters effect for air-cooled ejector cooling systems with R134a refrigerant. *Renew. Energy* **2012**, *46*, 155–163. [[CrossRef](#)]
19. Wu, H.Q.; Liu, Z.L.; Han, B. Numerical investigation of the influences of mixing chamber geometries on steam ejector performance. *Desalination* **2014**, *353*, 15–20. [[CrossRef](#)]
20. Yan, J.; Wen, N.; Wang, L.; Li, X.; Liu, Z.; Li, S. Optimization on ejector key geometries of a two-stage ejector-based multi-evaporator refrigeration system. *Energy Convers. Manag.* **2018**, *175*, 142–150. [[CrossRef](#)]
21. Li, C.; Li, Y.; Lei, W. Configuration dependence and optimization of the entrainment performance for gas–gas and gas–liquid ejectors. *Appl. Therm. Eng.* **2012**, *48*, 237–248. [[CrossRef](#)]

22. Li, C.; Li, Y.Z. Investigation of entrainment behavior and characteristics of gas–liquid ejectors based on CFD simulation. *Chem. Eng. Sci.* **2011**, *66*, 405–416. [[CrossRef](#)]
23. Kandakure, M.T.; Gaikar, V.G.; Patwardhan, A.W. Hydrodynamic aspects of ejectors. *Chem. Eng. Sci.* **2005**, *60*, 6391–6402. [[CrossRef](#)]
24. Balamurugan, S.; Gaikar, V.G.; Patwardhan, A.W. Effect of ejector configuration on hydrodynamic characteristics of gasliquid ejectors. *Chem. Eng. Sci.* **2008**, *63*, 721–731. [[CrossRef](#)]
25. Metin, C.; Gök, O.; Atmaca, A.U.; Ereğ, A. Numerical investigation of the flow structures inside mixing section of the ejector. *Energy* **2019**, *166*, 1216–1228. [[CrossRef](#)]
26. Zheng, L.X. Simulation and Experimental Study on Dynamic Characteristics of Transcritical CO₂ Ejector Refrigeration System. Ph.D. Thesis, Xi'an Jiaotong University, Xi'an, China, 2018.
27. NIST. *Reference Fluid Thermodynamic and Transport Properties Database (REFPROP)*; Version 9.0; U.S. Department of Commerce: Gaithersburg, MD, USA, 2002.
28. Liu, F.; Groll, E.A. Study of ejector efficiencies in refrigeration cycles. *Appl. Therm. Eng.* **2013**, *52*, 360–370. [[CrossRef](#)]
29. Liepmann, H.W.; Roshko, A. *Elements of Gasdynamics*, 1st ed.; John Wiley & Sons: New York, NY, USA, 1957; pp. 98–100.
30. Zheng, L.X.; Deng, J.Q. Research on CO₂ ejector component efficiencies by experiment measurement and distributed-parameter modeling. *Energy Convers. Manag.* **2017**, *142*, 244–256. [[CrossRef](#)]
31. Churchill, S.W. Friction factor equation spans all fluid flow regimes. *Chem. Eng.* **1977**, *84*, 91–92.
32. Hwang, Y. Comprehensive Investigation of a Carbon Dioxide Refrigeration Cycle. Ph.D. Thesis, University of Maryland, College Park, MA, USA, 1997.
33. Faraz, N.; Khan, Y.; Anjum, A.; Kahshan, M. Three-Dimensional Hydro-Magnetic Flow Arising in a Long Porous Slider and a Circular Porous Slider with Velocity Slip. *Mathematics* **2019**, *7*, 748. [[CrossRef](#)]
34. Banasiak, K.; Hafner, A.; Andresen, T. Experimental and numerical investigation of the influence of the two-phase ejector geometry on the performance of the R744 heat pump. *Int. J. Refrig.* **2012**, *35*, 1617–1625. [[CrossRef](#)]
35. Li, Y.; Deng, J. Numerical investigation on the performance of transcritical CO₂ two-phase ejector with a novel non-equilibrium CFD model. *Energy* **2022**, *238*, 121995. [[CrossRef](#)]
36. Elbel, S. Historical and present developments of ejector refrigeration systems with emphasis on transcritical carbon dioxide air-conditioning applications. *Int. J. Refrig.* **2011**, *34*, 1545–1561. [[CrossRef](#)]